

Modeling of microporosity formation and hydrogen concentration evolution during solidification of an Al-Si alloy

Qingyu Zhang(张庆宇), Dongke Sun(孙东科), Shunhu Zhang(章顺虎), Hui Wang(王辉), Mingfang Zhu(朱鸣芳)

Citation: Chin. Phys. B . 2020, 29(7): 078104 . **doi:** 10.1088/1674-1056/ab8abb
Journal homepage: http://cpb.iphy.ac.cn; http://iopscience.iop.org/cpb

What follows is a list of articles you may be interested in

Overview of finite elements simulation of temperature profile to estimate properties of materials 3D-printed by laser powder-bed fusion

Habimana Jean Willy, Xinwei Li(李辛未), Yong Hao Tan, Zhe Chen(陈哲), Mehmet Cagirici, Ramadan Borayek, Tun Seng Herng, Chun Yee Aaron Ong, Chaojiang Li(李朝将), Jun Ding(丁军)

Chin. Phys. B . 2020, 29(4): 048101 . **doi:** 10.1088/1674-1056/ab6d4e

Effect of AlN coating on hydrogen permeability and surface structure of VT6 alloy by vacuum arc ion plating

Zi-Yi Ding(丁子祎)

Chin. Phys. B . 2019, 28(10): 108101 . **doi:** 10.1088/1674-1056/ab3a8e

Cyclic stress induced phase transformation insuper-bainitic microstructure

Wencui Xiu(修文翠), Ying Han(韩英), Cheng Liu(刘澄), Hua Wu(吴化), Yunxu Liu(刘云旭)

Chin. Phys. B . 2017, 26(3): 038101 . **doi:** 10.1088/1674-1056/26/3/038101

Amorphous phase formation rules in high-entropy alloys

Qiu-Wei Xing(邢秋玮), Yong Zhang(张勇)

Chin. Phys. B . 2017, 26(1): 018104 . **doi:** 10.1088/1674-1056/26/1/018104

Influence of vacuum degree on growth of Bi_2Te_3 single crystal

Tang Yan-Kun, Zhao Wen-Juan, Zhu Hua-Qiang, Huang Yong-Chao, Cao Wei-Wei, Yang Qian, Yao Xiao-Yan, Zhai Ya, Dong Shuai

Chin. Phys. B . 2015, 24(7): 078101 . **doi:** 10.1088/1674-1056/24/7/078101

Modeling of microporosity formation and hydrogen concentration evolution during solidification of an Al–Si alloy*

Qingyu Zhang(张庆宇)[1,2,†], Dongke Sun(孙东科)[3], Shunhu Zhang(章顺虎)[1], Hui Wang(王辉)[4], and Mingfang Zhu(朱鸣芳)[2,‡]

[1] *Shagang School of Iron and Steel, Soochow University, Suzhou* 215137, *China*
[2] *Jiangsu Key Laboratory for Advanced Metallic Materials, School of Materials Science and Engineering, Southeast University, Nanjing* 211189, *China*
[3] *Jiangsu Key Laboratory for Design and Manufacture of Micro-Nano Biomedical Instruments, School of Mechanical Engineering, Southeast University, Nanjing* 211189, *China*
[4] *State Key Laboratory for Advanced Metals and Materials, University of Science and Technology Beijing, Beijing* 100083, *China*

(Received 23 December 2019; revised manuscript received 4 March 2020; accepted manuscript online 18 April 2020)

We simulate the evolution of hydrogen concentration and gas pore formation as equiaxed dendrites grow during solidification of a hypoeutectic aluminum–silicon (Al–Si) alloy. The applied lattice Boltzmann-cellular automaton-finite difference model incorporates the physical mechanisms of solute and hydrogen partitioning on the solid/liquid interface, as well as the transports of solute and hydrogen. After the quantitative validation by the simulation of capillary intrusion, the model is utilized to investigate the growth of the equiaxed dendrites and hydrogen porosity formation for an Al–(5 wt.%)Si alloy under different solidification conditions. The simulation data reveal that the gas pores favorably nucleate in the corners surrounded by the nearby dendrite arms. Then, the gas pores grow in a competitive mode. With the cooling rate increasing, the competition among different growing gas pores is found to be hindered, which accordingly increases the pore number density in the final solidification microstructure. In the late solidification stage, even though the solid fraction is increasing, the mean concentration of hydrogen in the residue melt tends to be constant, corresponding to a dynamic equilibrium state of hydrogen concentration in liquid. As the cooling rate increases or the initial hydrogen concentration decreases, the temperature of gas pore nucleation, the porosity fraction, and the mean porosity size decrease, whilst the mean hydrogen concentration in liquid increases in the late solidification stage. The simulated data present identical trends with the experimental results reported in literature.

Keywords: microporosity, solidification microstructure, modeling, lattice Boltzmann method

PACS: 81.05.Bx, 81.30.–t, 47.55.D–, 47.61.Jd **DOI:** 10.1088/1674-1056/ab8abb

1. Introduction

With the demands for light weight in automobiles and aircrafts, the application of aluminum alloys in these industries increases greatly. For aluminum alloy castings, the formation of microporosity is one of the most detrimental defects occurred in the solidification process.[1–4] The mechanical properties of the castings, particularly the fatigue resistance, could be reduced significantly due to the presence of the porosity defects.[4] Accordingly, the research of microporosity generation in aluminum alloy castings has collected extensive attention from the industrial production and academic study. Owing to the different porosity formation mechanisms, the microporosity defects can be categorized to shrinkage porosity and gas porosity. The former is caused by insufficient feeding of the melt because the permeability of the mush zone decreases with the solid fraction increasing, while the latter is produced due to the evolution of insoluble hydrogen gas in liquid during solidification.[4]

Numerous studies have been carried out to explore the mechanisms of gas pore formation through experimental observation and theoretical analyses.[5–12] The techniques of *in situ* observation for transparent organic materials using optical microscopy and for aluminum alloys using x-ray radiography provided a great deal of meaningful information, including the images of gas bubble emergence, bubble–dendrite interaction, bubble morphological evolution, and bubble movement.[5–7] Since the formation of gas bubbles in aluminum alloys is dependent on the variations of the local hydrogen concentrations and hydrogen solubility in melt, it is vital to obtain temporal and spatial evolution of hydrogen distributions in melts as solidification occurs. However, real-time quantitative determination of hydrogen concentration in aluminum alloy melts during solidification is so far unavailable. In the aspects of theoretical study, mathematical models were proposed and focused on the prediction of quantitative data under different conditions, such as porosity percentage and porosity size.[8–12] Yet, those models are incapable of providing the graphical morphologi-

*Project supported by the National Natural Science Foundation of China (Grant No. 51901148), the Fund of the State Key Laboratory of Solidification Processing (Northwestern Polytechnical University), China (Grant No. SKLSP202006), and the State Key Lab of Advanced Metals and Materials (University of Science and Technology Beijing), China (Grant No. 2019-Z15).

†Corresponding author. E-mail: qingyu.zhang@suda.edu.cn
‡Corresponding author. E-mail: zhumf@seu.edu.cn

© 2020 Chinese Physical Society and IOP Publishing Ltd

cal output of the microporosity and dendritic microstructure.

Nowadays, owing to the rapid development in the area of computing techniques, numerical modeling has emerged as an important complementary approach for the study of microstructural evolution in the process of alloy solidification. Numerical modeling not only reproduces the dynamic evolution of the solid fraction and concentration fields, but also fills the technical gap between the data obtained from experimental observations and theoretical analyses.[13–15] Various computational models based on cellular automaton (CA) and phase-field methods have been developed for simulating the formation and development of microporosity as the dendrites grow.[16–21] The simulation results have revealed the irregular shape of gas porosity affected by the nearby dendrites,[16] morphological variation of the growing bubbles and columnar dendrites after confronting each other,[17] formation of multiple gas pores in the process of welding of an Al–Cu alloy,[18] and gas porosity formation together with the equiaxed grains.[19,20] We previously developed a CA model for simulating hydrogen porosity formation in the dendritic and eutectic solidification stages for an Al–Si alloy.[21] The regimes of the hydrogen gas pores in the entire solidification processes were reasonably presented. In the above-mentioned simulations, however, the gas pore nuclei were either placed arbitrarily in the domain or generated by the stochastic model. As a result, some levels of artificial effects were inevitably introduced in the simulations, such as the number and position of the gas pore nuclei.

In past decades, the lattice Boltzmann (LB) models have been widely applied for simulating various multi-phase phenomena involving the gas/liquid/solid (G/L/S) phases.[22,23] By utilizing the nature of the multi-phase LB models for describing the interactions between fluid particles, the nucleation of a fluid phase in another phase owing to the evolution of the surrounding environment can be simulated.[24,25] The multi-phase LB models were coupled with the CA approach for modeling gas bubble formation as aluminum alloy solidification takes place,[26–28] in which the nucleation, movement, and merging of the growing bubbles during dendritic solidification could be visualized. However, these models have not encompassed the mechanism of hydrogen partitioning as dendrites grow. Recently, we developed a coupled model by combining the LB, CA, and finite difference (FD) methods to investigate the emergence of gas bubbles as the equiaxed and columnar dendrites grow for an Al–Cu alloy.[29] The LB-CA-FD model takes the effect of hydrogen partitioning into consideration, and this model has the capability of reasonably describing the evolution of hydrogen concentration as bubbles and dendrites grow. However, the influences of solidification conditions, such as cooling rate and initial hydrogen concentration, on gas pore formation and dendrite growth have not been investigated exhaustively.

In the present study, the LB-CA-FD model is utilized to simulate the nucleation and growth of hydrogen gas pores during dendritic solidification of an Al–(5 wt.%)Si alloy. This model could reproduce the hydrogen concentration variations, nucleation of the gas pores, and the morphological evolution of the growing hydrogen porosities and dendrites. The effects of cooling rate and the initial concentration of hydrogen in the Al–(5 wt.%)Si melt on gas pore nucleation and growth are investigated. Comparisons between the simulation results and the experimental data are performed for better understanding the effects of the various factors on microporosity formation.

2. Model description and governing equations

In the recently proposed LB-CA-FD model, essentially the LB model describes the hydrogen concentration evolution and the features of bubble flows, while the CA-FD model calculates the dendrite growth and solute diffusion.[29] In the present study, the solidification shrinkage is not considered, and the effect of convection is neglected.

For the multi-relaxation-time (MRT) multi-phase LB model, the transport of hydrogen atoms is described by the evolution of the distribution functions, which is written as[23]

$$\begin{aligned} &f_i(\boldsymbol{x}+\boldsymbol{e}_i\Delta t, t+\Delta t) - f_i(x,t) \\ &= -\left(\boldsymbol{M}^{-1}\boldsymbol{\Lambda}\boldsymbol{M}\right)_{ij}\left(f_j - f_j^{\mathrm{eq}}\right) + F_i'\Delta t, \quad i,j=0,1,\ldots,8, \end{aligned} \tag{1}$$

where f_i is the distribution function, and f_i^{eq} represents the equilibrium distribution function; $\boldsymbol{x}$ and t represent the position and time, and Δt is the time step. The microscopic velocities $\boldsymbol{e}_i$ and the orthogonal transformation matrix $\boldsymbol{M}$ read

$$\boldsymbol{e}_i = c\cdot\begin{bmatrix} 0 & 1 & 0 & -1 & 0 & 1 & -1 & -1 & 1 \\ 0 & 0 & 1 & 0 & -1 & 1 & 1 & -1 & -1 \end{bmatrix}, \tag{2}$$

$$\boldsymbol{M} = \begin{bmatrix} 1 & 1 & 1 & 1 & 1 & 1 & 1 & 1 & 1 \\ -4 & -1 & -1 & -1 & -1 & 2 & 2 & 2 & 2 \\ 4 & -2 & -2 & -2 & -2 & 1 & 1 & 1 & 1 \\ 0 & 1 & 0 & -1 & 0 & 1 & -1 & -1 & 1 \\ 0 & -2 & 0 & 2 & 0 & 1 & -1 & -1 & 1 \\ 0 & 0 & 1 & 0 & -1 & 1 & 1 & -1 & -1 \\ 0 & 0 & -2 & 0 & 2 & 1 & 1 & -1 & -1 \\ 0 & 1 & -1 & 1 & -1 & 0 & 0 & 0 & 0 \\ 0 & 0 & 0 & 0 & 0 & 1 & -1 & 1 & -1 \end{bmatrix}, \tag{3}$$

where $c = \Delta x/\Delta t$ is the lattice speed with Δx representing the lattice size. The lattice speed is $c = 1$ in the present work, since the lattice size and time step are assigned as $\Delta x = 1$ and $\Delta t = 1$, respectively. In Eq. (1), $\boldsymbol{M}^{-1}$ is the inverse matrix of $\boldsymbol{M}$, and F_i' is the forcing term. The diagonal matrix $\boldsymbol{\Lambda}$ consists of different relaxation times, defined as

$$\boldsymbol{\Lambda} = \mathrm{diag}\left(\tau_\rho^{-1}, \tau_e^{-1}, \tau_\zeta^{-1}, \tau_j^{-1}, \tau_q^{-1}, \tau_j^{-1}, \tau_q^{-1}, \tau_\nu^{-1}, \tau_\nu^{-1}\right), \tag{4}$$

where $\tau_\rho = 1.0$, $\tau_j = 1.0$, $\tau_\nu = 1.0$, $\tau_e = 1.25$, $\tau_\zeta = 1.25$, and $\tau_q = 0.91$ are employed in this work according to the previous studies.[23,29]

The distribution functions in the moment space are obtained by $\boldsymbol{m}=\boldsymbol{M}\boldsymbol{f}$ and $\boldsymbol{m}^{\rm eq}=\boldsymbol{M}\boldsymbol{f}^{\rm eq}$, in which the distribution functions are written in vector forms. We can write $\boldsymbol{m}^{\rm eq}$ as

$$\begin{aligned}\boldsymbol{m}^{\rm eq} = \rho[&1,-2+3|u|^2,1-3|u|^2,\\ &u_x,-u_x,u_y,-u_y,u_x^2-u_y^2,u_xu_y]^{\rm T},\end{aligned} \tag{5}$$

where ρ and $\boldsymbol{u}=[u_x,u_y]^{\rm T}$ are the macroscopic density and velocity, evaluated by $\rho=\sum_i f_i$ and $\rho\boldsymbol{u}=\sum_i \boldsymbol{e}_i f_i+\boldsymbol{F}\Delta t/2$, respectively. $\boldsymbol{F}$ is the forcing term in the velocity space.

After the linear transformation of Eq. (1) from the velocity space to the moment space, the LB equation is

$$\boldsymbol{m}^*=\boldsymbol{m}-\boldsymbol{\Lambda}(\boldsymbol{m}-\boldsymbol{m}^{\rm eq})+\Delta t\left(\boldsymbol{I}-\frac{\boldsymbol{\Lambda}}{2}\right)\boldsymbol{S}, \tag{6}$$

where $\boldsymbol{I}$ and $\boldsymbol{S}$ are the unit tensor and the forcing term in the moment space. $\boldsymbol{S}$ and $\boldsymbol{F}'$ are matched by $(\boldsymbol{I}-\boldsymbol{\Lambda}/2)\boldsymbol{S}=\boldsymbol{M}\boldsymbol{F}'$, and $\boldsymbol{F}'$ is the vector form of F_i' in Eq. (1). In the velocity space, the propagation step of the fluid particles is described by

$$f_i(x+e_i\Delta t,t+\Delta t)=f_i^*(x,t)+\omega_i' E, \tag{7}$$

where $\boldsymbol{f}^*=\boldsymbol{M}^{-1}\boldsymbol{m}^*$ is the relationship between the distribution functions in the moment space and in the velocity space. The weight coefficients are $\omega_i'=4/9$ for $|e_i|^2=0$, $\omega_i'=1/9$ for $e_i|^2=1$, and $\omega_i'=1/36$ for $|e_i|^2=2$. E is a source term representing the hydrogen amount rejected by the moving S/L interface (see Eq. (16)).

$\boldsymbol{S}$ in Eq. (6) is calculated by

$$\begin{aligned}\boldsymbol{S} = [&0,6\boldsymbol{u}\cdot\boldsymbol{F}+12\varepsilon|\boldsymbol{F}|^2/\left(\psi^2\Delta t(\tau_e-0.5)\right),-6\boldsymbol{u}\cdot\boldsymbol{F}\\ &-12\varepsilon|\boldsymbol{F}|^2/\left(\psi^2\Delta t(\tau_\zeta-0.5)\right),F_x,-F_x,F_y,-F_y,\\ &2\left(u_xF_x-u_yF_y\right),u_xF_y+u_yF_x]^{\rm T},\end{aligned} \tag{8}$$

where $\varepsilon=0.084$ determines the mechanical stability condition.[23,29] The force is written as $\boldsymbol{F}=\boldsymbol{F}_{\rm c}+\boldsymbol{F}_{\rm ads}$, where $\boldsymbol{F}_{\rm c}$ is the force acting between the neighboring fluid nodes, and $\boldsymbol{F}_{\rm ads}$ is the force acting between the fluid and solid nodes. $\boldsymbol{F}_{\rm c}$ and $\boldsymbol{F}_{\rm ads}$ are defined by[23]

$$\boldsymbol{F}_{\rm c}(\boldsymbol{x},t)=-G_{\rm c}\psi(\boldsymbol{x},t)\sum_i\omega_i\psi(\boldsymbol{x}+\boldsymbol{e}_i\Delta t,t)\boldsymbol{e}_i, \tag{9}$$

$$\boldsymbol{F}_{\rm ads}(\boldsymbol{x},t)=-G_{\rm ads}\psi^2(\boldsymbol{x},t)\sum_i\omega_i s(\boldsymbol{x}+\boldsymbol{e}_i\Delta t,t)\boldsymbol{e}_i, \tag{10}$$

where $G_{\rm c}$ and $G_{\rm ads}$ are the fluid-fluid interaction and fluid-solid adhesion parameter that coherently tune the wettability; ω_i are the weight coefficients for the force calculations, and the values are $\omega_i=1/3$ for $|e_i|^2=1$ and $\omega_i=1/12$ for $|e_i|^2=2$; $s(\boldsymbol{x}+\boldsymbol{e}_i\Delta t)$ is an indicator function for indicating a solid ($s=1$) or a fluid ($s=0$) nearest node. The pseudopotential function ψ is given by

$$\psi=\sqrt{2(P_{\rm EOS}-\rho c_{\rm s}^2)/G_{\rm c}}, \tag{11}$$

where $c_{\rm s}=1/\sqrt{3}$ is the lattice sound speed. $P_{\rm EOS}$ is the equation of state,[23]

$$P_{\rm EOS}=\begin{cases}\rho\theta_1, & \rho\leqslant\rho_{\rm s1},\\ \rho_{\rm s1}\theta_1+(\rho-\rho_{\rm s1})\theta_M, & \rho_{\rm s1}<\rho\leqslant\rho_{\rm s2},\\ \rho_{\rm s1}\theta_1+(\rho_{\rm s2}-\rho_{\rm s1})\theta_M+(\rho-\rho_{\rm s2})\theta_2, & \rho>\rho_{\rm s2},\end{cases} \tag{12}$$

where $\theta_1=0.64c_{\rm s}^2$, $\theta_2=c_{\rm s}^2$, and $\theta_M=-0.16c_{\rm s}^2$ are adopted. By setting $\rho_1=1$ and $\rho_2=50$ in the present work, the values of $\rho_{\rm s1}$ and $\rho_{\rm s2}$ are obtained by solving the equations for mechanical and chemical equilibriums, and the results are $\rho_{\rm s1}=1.81$ and $\rho_{\rm s2}=43.8$, respectively. In the LB simulations, the periodic boundary condition is applied on all walls of the domain. A bounce-back rule is adopted on the fluid-solid boundaries.

The CA-FD model is briefly described as follows. Within each time step, the variation of solid fraction in an S/L interface cell is evaluated by[13]

$$\Delta f_{\rm s}=g\cdot\frac{C_{\rm l}^{\rm eq}-C_{\rm l}^*}{C_{\rm l}^{\rm eq}\left(1-k_{\rm p}\right)}, \tag{13}$$

where g and $C_{\rm l}^{\rm eq}$ are the geometrical factor and local equilibrium liquid concentration. $C_{\rm l}^{\rm eq}$ is calculated by

$$C_{\rm l}^{\rm eq}=\frac{T^*-T_{\rm m}}{m_{\rm l}}+\frac{\Gamma\cdot[1-15\varepsilon\cos(4(\varphi-\theta_0))]\cdot\bar{K}}{m_{\rm l}}, \tag{14}$$

where T^* and $T_{\rm m}$ are the local temperature and the melting point of the pure solvent, respectively; $m_{\rm l}$ is the liquidus slope, and Γ is the Gibbs–Thomson coefficient; ε is the degree of anisotropy of the surface energy; φ is the growth angle between the normal to the S/L interface and the x-axis, and θ_0 is the angle of the preferential growth direction with respect to the x-axis. The calculations of the geometrical factor g and the local interfacial curvature K can be found elsewhere.[13,29]

In Eq. (13), the local actual liquid concentration $C_{\rm l}^*$ is obtained by solving the diffusion equation

$$\frac{\partial C_j}{\partial t}=\nabla\cdot(D_j\nabla C_j)+C_j\left(1-k_{\rm p}\right)\frac{\partial f_{\rm s}}{\partial t}, \tag{15}$$

where C_i is the concentration, and D_i is the diffusion coefficient. The amount of solute atoms rejected by the migrating S/L interface caused by solute partitioning is represented by the second term on the right-hand side. The subscript j is written as s or l for denoting solid or liquid nodes. Equation (15) could be solved by either the LB method or the FD method.[30,31] Nevertheless, in the present work, Eq. (15) is solved by the FD method in the explicit manner. There are two reasons for choosing the FD method: (i) The FD method needs less memory than the LB method. (ii) In the simulation of dendrite growth under the pure diffusion condition, it is convenient for the FD method to calculate solute diffusion using different diffusion coefficients in liquid, solid, and S/L

interface, while it is a non-trivial issue for the LB method. In the calculations, the time step is taken as $\Delta t = \Delta x^2/(4.5D_l)$. A zero-flux boundary condition is implemented on the boundary nodes.

Table 1. Physical and thermodynamic properties of Al–Si alloys.[21]

Symbol	Definition	Value	Unit
Γ	Gibbs–Thomson coefficient	1.7×10^{-7}	°C·m
T_m	Melting temperature of the pure Al	660.452	°C
D_l	Diffusion coefficient of solute Si in liquid	4.3×10^{-9}	m^2/s
D_s	Diffusion coefficient of solute Si in solid	4.3×10^{-13}	m^2/s
K_H	Partition coefficient of H	0.069	–
m	Slope of the liquidus line	−6.0	°C/wt.%
k_p	Partition coefficient of solute Si	0.117	–

The effects of gas pore-dendrite interaction and hydrogen partitioning provide the connection between the multi-phase LB model and the CA-FD model. The hydrogen amount rejected at the S/L interface is incorporated into the multi-phase LB model through the source term in Eq. (7), which is defined by

$$E = \frac{1}{(\Delta t_{\mathrm{CA-FDM}}/\Delta t_{\mathrm{LB}})} C_{\mathrm{H}}^{*}(1-k_{\mathrm{H}})\frac{\partial f_s}{\partial t}, \tag{16}$$

where k_H and C_H^* are the hydrogen partitioning coefficient and the local hydrogen concentration in liquid, respectively. $\Delta t_{\mathrm{CA-FD}}$ and Δt_{LB} are the time steps of the CA-FD model and the LB model, respectively. Considering that hydrogen transport is faster than solute diffusion, $\Delta t_{\mathrm{CA-FD}}/\Delta t_{\mathrm{LB}} > 1$ is adopted. Corresponding to the previous work,[29] $\Delta t_{\mathrm{CA-FD}}/\Delta t_{\mathrm{LB}} = 3$ is used in the present study. In fact, the algorithm for the calculation of the rejected hydrogen amount due to the partitioning effect is similar to that of the rejected amount of solute atoms during solidification. Therefore, apart from the term of time step ratio, the rest part of Eq. (16) is comparable to the second term on the right-hand side of Eq. (15).

The physical and thermodynamic parameters of Al–Si alloys used in the simulations are displayed in Table 1.

3. Results and discussion

3.1. Model validation

In our previous study, the proposed LB-CA-FD model was verified by the Laplace law test and contact angle simulation.[29] In order to further validate its capability for modeling the fluid dynamics in a complex system involving the G/L/S phases, the dynamic process of capillary intrusion is simulated. In this process, the wetting fluid phase migrates in a capillary tube since a pressure difference exists on two sides of the curved fluid-fluid interface. The simulated data are compared with a theoretical model applied in the work of Liu *et al.*[32] In the analytical model, the position of the migrating curved fluid-fluid interface in a capillary tube, ξ, is a function of time t,

$$\begin{aligned} \gamma\cos\theta &= \frac{6}{r}\left[\mu_{\mathrm{wetting}}\xi + \mu_{\mathrm{non-wetting}}(L-\xi)\right]\frac{\mathrm{d}\xi}{\mathrm{d}t}, \\ \xi|_{t=0} &= \xi_0, \end{aligned} \tag{17}$$

where γ is the surface tension; θ is the intrinsic contact angle of the wetting fluid; r and L are the width and length of the capillary tube; μ_{wetting} and $\mu_{\mathrm{non-wetting}}$ are the dynamic viscosities of the wetting and non-wetting fluid phases, respectively; ξ_0 is the interface position at the initial time.

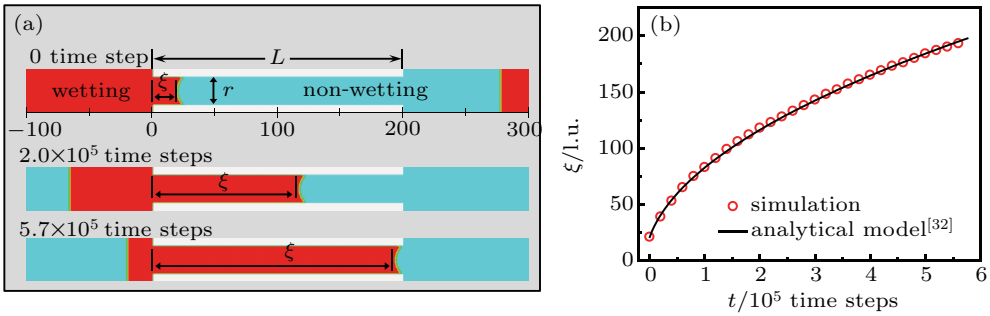


Fig. 1. Time evolution of (a) the simulated wetting and non-wetting fluids in the process of capillary intrusion; (b) fluid-fluid interface position ξ in the capillary tube, obtained from the simulation and the analytical prediction.[32]

In the simulation of capillary intrusion, the computation domain consists of 400×35 lattice units (l.u.). A horizontal capillary tube with a width of $r = 21$ l.u. and a length of $L = 200$ l.u. is set in the middle portion of the computation domain. As shown in Fig. 1(a), the wetting and non-wetting fluids are initialized in the capillary tube, and the initial interface position is $\xi_0 = 20$ l.u. By setting $G_{\mathrm{ads}} = -1.025$, the intrinsic contact angle of the wetting fluid is $\theta = 44.5°$. In this study, the arrangements of the intrinsic contact angle and the geometrical parameters of the capillary tube are identical to the work of Liu *et al.*[32] Other parameters of the wetting and non-wetting fluids are measured to be $\mu_{\mathrm{wetting}} = 8.36$, $\mu_{\mathrm{non-wetting}} = 0.19$, and $\gamma = 1.14$, respectively. Figure 1(a) displays the time evolution of the wetting fluid moving in the capillary tube obtained from the simulation. As is shown, the fluid-fluid interface presents a curved shape, and the wetting

fluid phase gradually intrudes into the capillary tube. Figure 1(b) presents the plots of the fluid-fluid interface position in the capillary tube as a function of time, obtained from the simulation (open circles) and the analytical model (solid line). Note that the simulated fluid-fluid interface position agrees well with the analytical prediction, demonstrating the correctness of the codes and the quantitative capability of the model for the simulation of multi-phase flows involving G/L/S phases.

3.2. Evolution of equiaxed dendrites and gas pores under different cooling rates

The simulations are carried out to investigate the growth of equiaxed dendrites and porosity formation as an Al–(5 wt.%)Si alloy solidifies under different cooling rates. The computational domain is composed of a 300×300 mesh, and the lattice unit and the mesh size are arranged as $\Delta x =$ 1 l.u. =3 μm. At the start, several initial equiaxed dendrites are set in the computational domain. The undercooling is arranged to be 3 °C, and the crystallographic orientations of the equiaxed dendrites are randomly generated. The initial concentration of hydrogen in the Al–(5 wt.%)Si melt is assigned as $C_{H0} = 0.022$. Figure 2 displays the simulated evolution of the equiaxed dendritic microstructure and gas bubble formation under the cooling rates (CR) of CR = 2 ℃/s (Figs. 2(a)–2(d)) and CR = 12 ℃/s (Figs. 2(e)–2(h)). Figure 2 is shown in the hydrogen concentration field. The numbers in the panels represent the local hydrogen concentrations, which are normalized by that in gas pores. As shown in Fig. 2(a), the concentration of hydrogen in the Al–(5 wt.%)Si melt exceeds the initial value. Clearly, this is caused by that the growing equiaxed dendrites reject hydrogen atoms into the nearby liquid nodes. Nevertheless, no gas pores emerge yet in Fig. 2(a), indicating that there exists an incubation period for hydrogen pore nucleation. As the solidification proceeds, some gas pores appear at the corners composed by the dendrite arms (Fig. 2(b)), which can be attributed to that the local hydrogen concentrations in these regions exceed the supersaturation for gas pore nucleation. Subsequently, the concentrations of hydrogen in the melt decrease, denoting that the hydrogen atoms enter the gas pores to sustain their growth. As shown in Figs. 2(c) and 2(d), gas pore morphologies are slightly changed after contacting dendrite arms. In addition, it is shown in Figs. 2(b)–2(d) that the number of the gas bubbles decreases, even though the porosity percentage keeps increasing with time. This denotes that the gas bubbles grow competitively, i.e., some gas bubbles growing by eliminating the other ones. In the case of CR = 12 ℃/s, the dendrites grow rapidly with finer and longer side arms as shown in Figs. 2(e)–2(h). The gas pores are also found to appear in the corners surrounded by the dendrite arms, but the number of the bubbles remains higher than that of CR = 2 ℃/s. As dendrites and bubbles grow, the hydrogen concentrations in liquid also decrease with time. When the solid fraction reaches $f_s = 0.68$, as compared in Figs. 2(d) and 2(h), the sizes of the gas pores in the higher cooling rate case are much smaller than those in the lower cooling rate case. The comparisons of the number and size of the gas pores in Fig. 2 indicate that the competitive growth among different gas pores can be influenced by cooling rate. As described in our previous articles,[21,29] the competitive growth of gas pores is related to the interaction among several factors, e.g., pore size, supersaturation of hydrogen in the melt, and local hydrogen concentration. The supersaturation of hydrogen in the melt required for gas pore growth increases with decreasing the pore size. As a result, in the melt with a fixed hydrogen concentration, the bigger gas pores are favorable to keep growing, whilst the smaller gas pores are inclined to shrink and may eventually disappear. In this process, the local hydrogen concentrations in liquid nearby the gas bubbles are governed by hydrogen transport in liquid. Since the higher cooling rate produces finer equiaxed dendrites and longer arms, a more complex dendritic network is formed. Thus, the process of hydrogen transport in the liquid phase can be blocked by the dendritic network to some extent in the two-dimensional domain. As a result, the growth of large gas pores becomes more difficult due to the insufficient hydrogen supplement in the isolated liquid regions. Likewise, the elimination of small gas pores is also restrained. In addition, the time for gas pore growth and elimination becomes shorter by applying a higher cooling rate. Therefore, the competitive growth between gas pores is hindered by a higher cooling rate. The simulated data in Fig. 2 reveal that the application of a lower cooling rate not only leads to coarser dendrites, but also produces larger gas pores in the microstructure. These two consequences are both detrimental to the mechanical properties of castings.

Figure 3 presents the simulated percentage of porosity and mean normalized concentration of hydrogen in the remaining Al–Si melt versus temperature under the cooling rates of CR = 2 °C/s (Figs. 2(a)–2(d)) and CR = 12 °C/s (Figs. 2(e)–2(h)), respectively. In Fig. 3(a), it is seen that the percentages of porosity remain zero in the incubation period before gas pores appearing. After gas bubbles nucleate, the porosity percentages rise abruptly. It is found that with a slower cooling rate, the nucleation of gas pores occurs at a relatively higher temperature, and thus the time for gas pore growth is longer. As a consequence, the percentage of porosity in the lower cooling rate case remains higher than that in the higher cooling rate case. In the late time, the growth rates of the porosity percentage decrease. In Fig. 3(b), the profiles reveal that the

mean normalized hydrogen concentrations in liquid drastically increase from the initial hydrogen concentration ($C_{H0} = 0.022$) after the solidification starts. The hydrogen concentrations decrease apparently when gas pores emerge due to the fact that it requires consuming a large number of hydrogen atoms when the gas pores nucleate and grow. Then, the hydrogen concentrations tend to be relatively stable in the residue liquid phase. This implies that the amount of rejected hydrogen atoms during solidification is approximately equivalent to that consumed by the gas pore growth, which is a dynamic equilibrium state for bubble growth. In this dynamic equilibrium state, the local hydrogen concentrations in the nearby liquid phase are slightly greater than the hydrogen supersaturations for the growing bubbles. Accordingly, the bubbles could grow, even though the growth rate decreases in the final period. It is noteworthy that in the late solidification stage the hydrogen concentration in liquid under a higher cooling rate is higher than that under a lower cooling rate. Obviously, it is correlated with that the porosity fraction is lower in the higher cooling rate case, and hence more hydrogen atoms could remain within the residue melt.

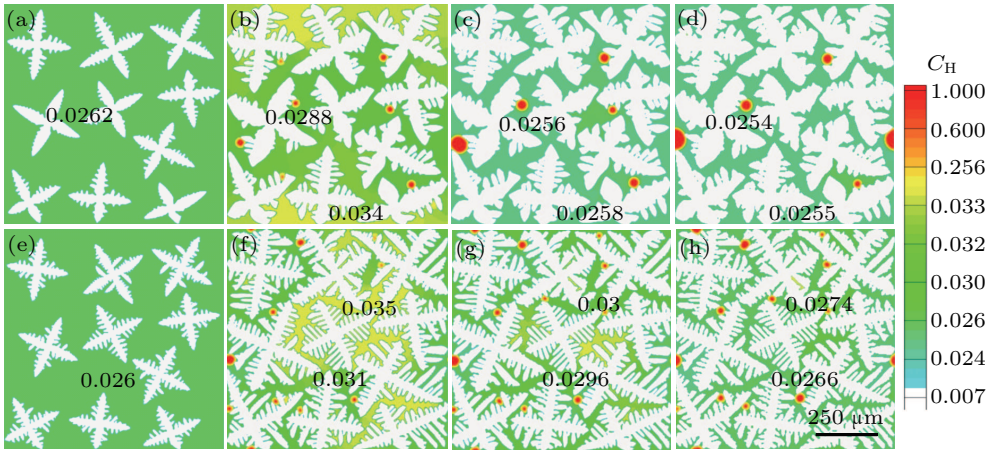


Fig. 2. Simulated equiaxed dendrite growth and gas pore formation for an Al–(5 wt.%)Si alloy under different cooling rates (CRs): (a)–(d) CR = 2 ℃/s; (a) $f_g = 0\%$, $f_s = 0.21$, $T = 621.2$ °C; (b) $f_g = 0.27\%$, $f_s = 0.51$, $T = 604.4$ °C; (c) $f_g = 0.96\%$, $f_s = 0.58$, $T = 596.0$ °C; (d) $f_g = 1.47\%$, $f_s = 0.68$, $T = 575.9$ °C; (e)–(h) CR = 12 °C/s; (e) $f_g = 0\%$, $f_s = 0.21$, $T = 613.7$ °C; (f) $f_g = 0.41\%$, $f_s = 0.59$, $T = 594.7$ °C; (g) $f_g = 0.64\%$, $F_s = 0.62$, $T = 591.0$ °C; (h) $f_g = 0.99\%$, $f_s = 0.68$, $T = 570.9$ °C. f_g, f_s, and T are the total porosity percentage, solid fraction, and temperature in the domain, respectively. The numbers in the panels indicate the local concentrations of hydrogen in the melt.

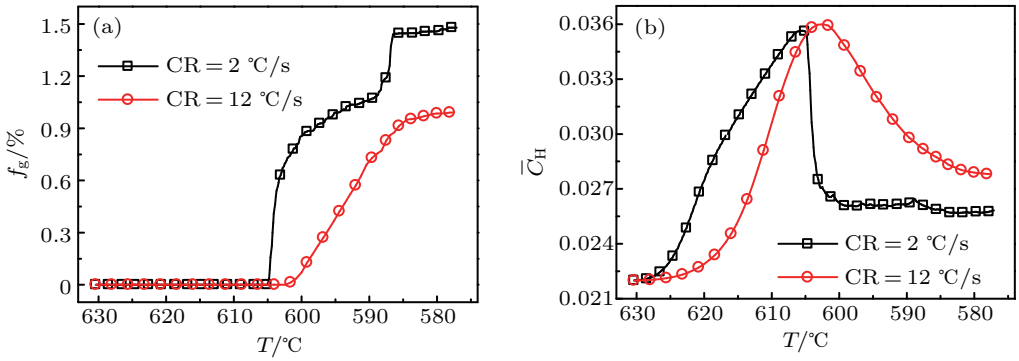


Fig. 3. Simulated curves of (a) percentage of porosity (f_g) and (b) mean normalized hydrogen concentration in the residue liquid phase ($\bar{C}_H$) as a function of temperature T with different CRs in the cases of Fig. 2.

Figure 4 displays the simulated final porosity percentage, mean pore radius, and pore number density varying with cooling rate. The initial normalized hydrogen concentrations in the simulations are arranged to be identical with Fig. 2. The simulated data of the final porosity percentage, mean pore radius, and pore number density are determined when the solid fractions reach 0.68. As shown in Fig. 4(a), the simulated final porosity percentage drops as the cooling rate increases, which presents identical trend with the experimental data for a hypoeutictic Al–Si alloy in the work of Carlson *et al.*[33] As shown in Fig. 4(b), with the cooling rate rising, the simulated mean pore radius decreases, whereas the pore number density increases. In the practical aluminum alloy casting process, the tensile and fatigue strengths of the casting components are drastically influenced by the porosity with a large size.[33] The simulated data in Fig. 4 show that the application of a higher cooling rate is favorable for reducing the porosity percentage and gas pore size, which is beneficial for elevating the mechanical properties of castings.

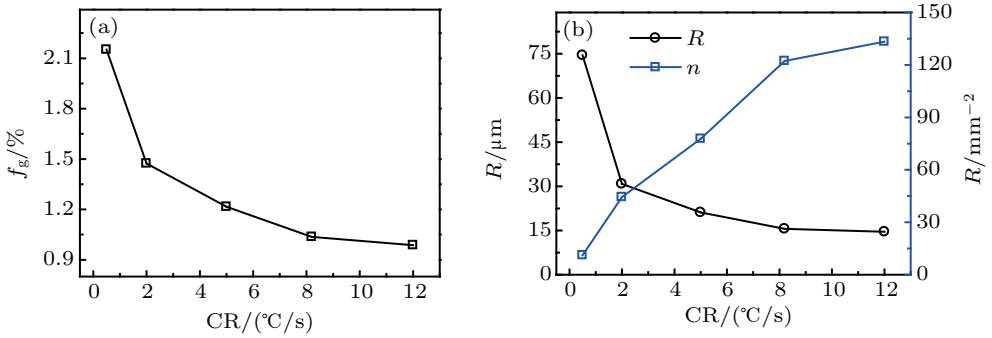


Fig. 4. Simulated (a) final percentage of porosity (f_g) and (b) mean pore radius (R) and pore number density (n) versus cooling rate (CR).

3.3. Gas pore formation under different initial hydrogen concentrations

The influence of initial concentration of hydrogen in the Al–Si melt on the solidification porosity formation for Al–(5 wt.%)Si is investigated using the present LB-CA-FD model. Figure 5 presents the simulated evolution of the equiaxed dendrite growth and gas pore formation with the initial hydrogen concentrations of $C_{H0} = 0.02$ (Figs. 5(a)–5(d)) and $C_{H0} = 0.026$ (Figs. 5(e)–5(h)), respectively. The cooling rate is fixed as CR = 12 °C/s, and other simulation parameters are identical with Fig. 2. The solid fractions of Figs. 5(a) and 5(e) are the same, but the hydrogen concentration in Fig. 5(e) is apparently higher. When the temperatures reach 608.0 °C (Figs. 5(b) and 5(f)), gas bubbles form near the dendrite arms in the case of $C_{H0} = 0.026$, but there appears to be no bubbles in the case of $C_{H0} = 0.02$ yet. Thus, the higher initial hydrogen concentration facilitates the nucleation of gas pores to be earlier during dendritic solidification. As seen in Figs. 5(c) and 5(g), the gas pore size in the case of $C_{H0} = 0.026$ is larger than that in the case of $C_{H0} = 0.02$. This is because the gas pores in Fig. 5(g) nucleate earlier, and they could grow in an extended period. The simulated data in Fig. 5 reveal that a greater initial hydrogen concentration tends to produce larger gas pores and higher pore number density in the final microstructure.

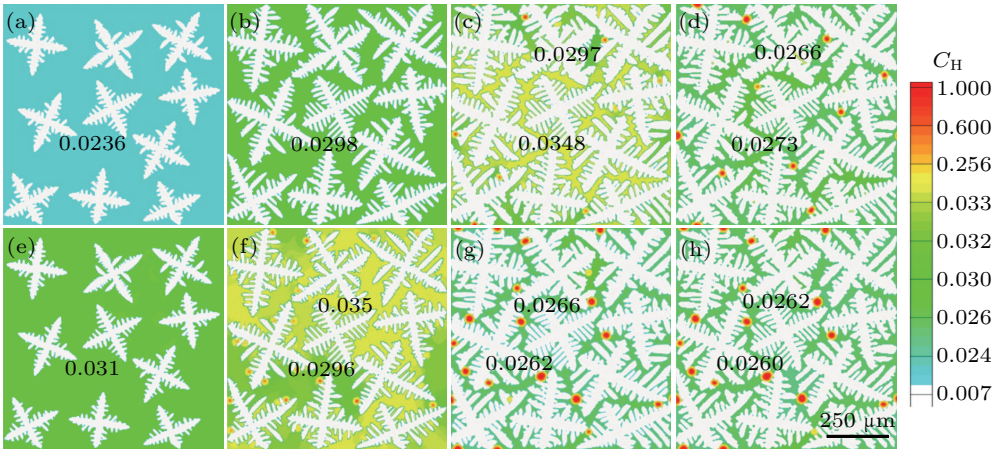


Fig. 5. Simulated equiaxed dendrite growth and gas pore formation for an Al–(5 wt.%)Si alloy with different initial hydrogen concentrations (C_{H0}): (a)–(d) $C_{H0} = 0.02$; (a) $f_g = 0\%$, $f_s = 0.21$, $T = 613.7$ °C; (b) $f_g = 0\%$, $f_s = 0.43$, $T = 608.0$ °C; (c) $f_g = 0.09\%$, $f_s = 0.65$, $T = 586.4$ °C; (d) $f_g = 0.66\%$, $f_s = 0.68$, $T = 570.9$ °C; (e)–(h) $C_{H0} = 0.026$; (e) $f_g = 0\%$, $f_s = 0.21$, $T = 613.7$ °C; (f) $f_g = 0.11\%$, $f_s = 0.43$, $T = 608.0$ °C; (g) $f_g = 1.86\%$, $f_s = 0.65$, $T = 586.4$ °C; (h) $f_g = 1.91\%$, $f_s = 0.68$, $T = 570.9$ °C. f_g, f_s, and T are the total porosity percentage, solid fraction, and temperature in the domain, respectively. The numbers in the panels indicate the local concentrations of hydrogen in the melt.

Figure 6 shows the plots of porosity percentages and mean hydrogen concentrations in the residue melt versus time and temperature for the cases of Fig. 5. In Fig. 6(a), it is seen that the incubation stage for bubble nucleation is shorter for the case with a higher initial concentration of hydrogen in the melt. After the gas bubbles emerge, the porosity percentages rise rapidly. It can be seen that as the solidification proceeds, the percentage of porosity for the case of $C_{H0} = 0.026$ remains apparently higher than that of $C_H = 0.02$. In Fig. 6(b), the curves of the mean hydrogen concentration increase with the declining temperature as the dendrites grow. Since the nucleation and growth of gas pores consume large amounts of hydrogen atoms in a short period, the mean hydrogen concentrations in liquid show abrupt drops after the gas pores emerge. Similar to Fig. 3(b), the mean hydrogen concentrations in the residue liquid phase tend to be relatively stable in the late stage, denoting that a dynamic equilibrium state is reached in this stage. In addition, Fig. 6(b) indicates that the mean hydrogen concentration in liquid during bubble growth in the case of a lower C_{H0} is slightly higher. As compared

in Figs. 5(d) and 5(h), the gas pores in the case of the lower C_{H0} are smaller, and thus require a greater hydrogen supersaturation in the nearby melt to sustain the growth of porosity. Therefore, when the dynamic equilibrium state is reached, the concentration of hydrogen in the Al–Si melt for the lower C_{H0} is accordingly higher.

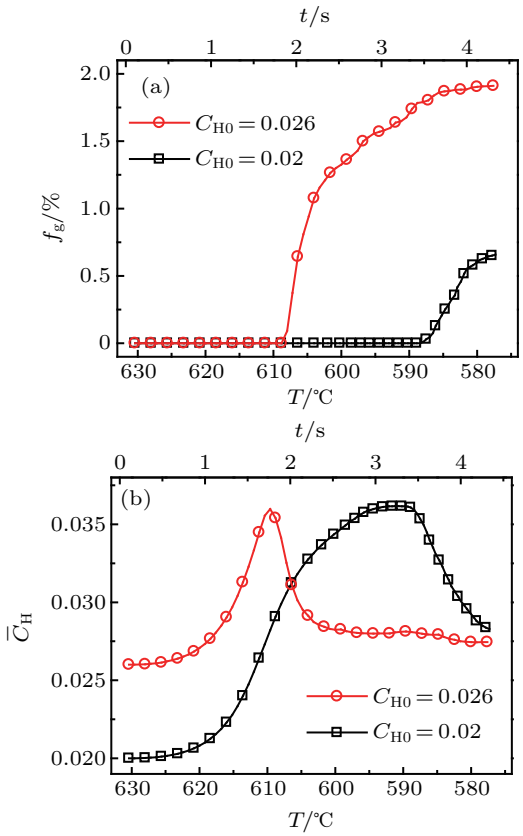


Fig. 6. Simulated curves of (a) porosity percentage (f_g) and (b) mean normalized concentration of hydrogen in residue melt ($\bar{C}_H$) versus time t and temperature T for different initial hydrogen concentrations C_{H0} in the cases of Fig. 5.

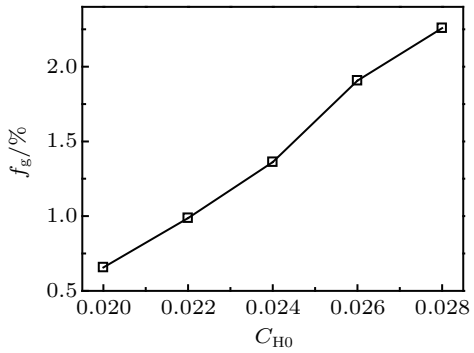


Fig. 7. Simulated final porosity percentage (f_g) versus initial hydrogen concentration C_{H0} for an Al–(5 wt.%)Si alloy.

Figure 7 presents the plot of the simulated final porosity percentage versus the initial concentration of hydrogen in the melt. In the simulations, the cooling rates are fixed to be CR = 12 °C/s. Apparently, the simulation result shows that the final porosity percentage increases as the initial concentration of hydrogen in the melt increases, which is identical to the trend of the plots obtained from the experiments for an Al–(7 wt.%)Si–(10 wt.%)SiC alloy in the work of Samuel and Samuel.[34] The simulation results in Fig. 7 reveal that the process of degassing is necessarily vital for decreasing the initial hydrogen concentration and thus to reduce the final porosity percentage of aluminum alloy castings.

4. Conclusions

The equiaxed dendrite growth and gas pore formation during hypoeutectic Al–Si alloy solidification is simulated using a previously proposed LB-CA-FD model. In this model, the hydrogen concentration variation as well as the gas pore nucleation and gas pore growth are described by the multiphase LB model, whilst the growth of dendrites and solute transport are described by the CA-FD model.

The present model is validated by simulating the dynamic process of capillary intrusion of the wetting liquid phase. The simulated profile of the curved fluid-fluid interface position varying with time is in good agreement with the analytical prediction, revealing the capability of the present model for reasonably describing the interactions between different phases.

The phenomena of gas bubble formation and dendrite growth with different cooling rates and initial hydrogen concentrations are simulated using the LB-CA-FD model. The hydrogen concentrations increase as the solidification proceeds. When the hydrogen concentrations exceed a certain level, the gas pores favorably appear in the corners surrounded by dendrite arms. Then, the gas pores start to grow, and a competitive growth mode is observed among the gas pores with various radii. The simulations visualize the evolution and distribution of hydrogen concentrations during gas pore and dendrite growth, which is coherently affected by hydrogen rejection as dendrites grow and the hydrogen consumption by gas pore nucleation and growth. It is found that the mean hydrogen concentrations in the residue melt become relatively stable as the equiaxed dendrites and gas pores grow, leading to a dynamic equilibrium state for the amount of hydrogen atoms in the residue melt. In this stage, the mean hydrogen concentration remains slightly higher when a higher cooling rate or a lower initial hydrogen concentration is applied. With the increase of cooling rate, the gas pores nucleate at a higher temperature. Moreover, as the cooling rate increases, the final percentage of porosity and mean pore radius decrease, whereas the porosity density increases. As the initial hydrogen concentration increases, the gas pores emerge earlier, and both the final porosity percentage and mean pore radius increase. The tendencies of the simulated porosity percentages varying with cooling rate and initial hydrogen concentration are identical with the experimental results. The simulated data reveal that applying a higher cooling rate and decreasing the initial concentration of hydrogen in the aluminum alloy melt through the

degassing process are beneficial for reducing the final porosity percentage of the aluminum alloy castings.

References

[1] Kurz W, Fisher D J and Trivedi R 2019 *Inter. Mater. Rev.* **64** 311
[2] Ding Z, Hu Q, Lu W, Ge X, Cao S, Sun S, Yang T, Xia M and Li J 2019 *J. Mater. Sci. Technol.* **35** 1388
[3] Yamamoto T and Komarov S V 2019 *Int. J. Cast Met. Res.* **32** 266
[4] Stefanescu D M 2005 *Int. J. Cast Met. Res.* **18** 129
[5] Xing H, Wang J, Chen C, Shen Z and Zhao C 2012 *J. Cryst. Growth* **338** 256
[6] Huang W D and Wang L L 2012 *Sci. Chin. Technol. Sci.* **55** 377
[7] Sun S, Hu Q, Lu W, Ding Z, Xia M and Li J 2018 *Metall. Mater. Trans. A* **49** 4429
[8] Khalajzadeh V, Goettsch D D and Beckermann C 2019 *Metall. Mater. Trans. A* **50** 757
[9] Bahmani A, Hatami N, Varahram N, Davami P and Shabani M O 2013 *Int. J. Adv. Manuf. Technol.* **64** 1313
[10] Gao Z M, Jie W Q, Liu Y Q, Zheng Y J and Luo H J 2019 *J. Alloy. Compd.* **797** 514
[11] Bhagavath S, Cai B, Atwood R, Li M, Ghaffari B, Lee P D and Karagadde S 2019 *Metall. Mater. Trans. A* **50** 4891
[12] Gao Z, Jie W, Liu Y and Luo H 2017 *Acta Mater.* **127** 277
[13] Zhu M and Stefanescu D 2007 *Acta Mater.* **55** 1741
[14] Xing H, Ankit K, Dong X, Chen H and Jin K 2018 *Int. J. Heat Mass Transfer* **117** 1107
[15] Xing H, Ji M, Dong X, Wang Y, Zhang L and Li S 2020 *Mater. Design* **185** 108250
[16] Meidani H, Jacot A and Rappaz M 2015 *Metall. Mater. Trans. A* **46** 23
[17] Du L, Wang L, Zheng B and Du H 2016 *Comput. Mater. Sci.* **114** 94
[18] Gu C, Wei Y, Yu F, Liu X and She L 2017 *Metall. Mater. Trans. A* **48** 4314
[19] Savithri S and Sasikumar R 2018 *Trans. Indian Inst. Met.* **71** 2657
[20] Hu Y, Xie J, Liu Z, Ding Q, Zhu W, Zhang J and Zhang W 2018 *Comput. Mater. Sci.* **142** 244
[21] Zhang Q, Wang T, Yao Z and Zhu M 2018 *Materialia* 4C **211**
[22] Chen L, Kang Q, Mu Y, He Y L and Tao W Q 2014 *Int. J. Heat Mass Transfer* **76** 210
[23] Li Q, Luo K H, Kang Q J and Chen Q 2014 *Phys. Rev. E* **90** 053301
[24] Li Q, Yu Y, Zhou P and Yan H J 2018 *Appl. Therm. Eng.* **132** 490
[25] Zhang Q, Sun D, Zhang Y and Zhu M 2014 *Langmuir* **30** 12559
[26] Wu W, Zhu M F, Sun D K, Dai T, Han Q Y and Raabe D 2012 *IOP Conf. Ser.: Mater. Sci. Eng.* **33** 012103
[27] Sun D, Zhu M, Wang J and Sun B 2016 *Int. J. Heat Mass Transfer* **94** 474
[28] Nabavizadeh S, Eshraghi M and Felicelli S 2019 *Appl. Sci.* **9** 57
[29] Zhang Q, Sun D, Pan S and Zhu M 2020 *Int. J. Heat Mass Transfer* **146** 118838
[30] Chai Z, Sun D, Wang H and Shi B 2018 *Int. J. Heat Mass Transfer* **122** 631
[31] Chai Z, Liang H, Du R and Shi B 2019 *SIAM J. Sci. Comput.* **41** B746
[32] Liu H, Ju Y, Wang N, Xi G and Zhang Y 2015 *Phys. Rev. E* **92** 033306
[33] Carlson K D, Lin Z and Beckermann C 2007 *Metall. Mater. Trans. B* **38** 541
[34] Samuel A M and Samuel F H 1993 *Metall. Trans. A* **24** 1857